Aqueous phase conversion of CO_2 into acetic acid over thermally transformed MIL-88B

Waqar Ahmad
Monash University
Paramita Koley
Monash University
Swarit Dwivedi
Monash University
Abhijit Shrotri
Hokkaido University
Akshat Tanksale (akshat.tanksale@monash.edu)
Monash University https://orcid.org/0000-0002-7087-0912

Article

Keywords: Methanol hydrocarboxylation, CO2 transformation, Acetic acid, Formic acid, Thermally transformed MOFs

Posted Date: November 10th, 2021

DOI: https://doi.org/10.21203/rs.3.rs-1029433/v1

Version of Record: A version of this preprint was published at Nature Communications on May 17th, 2023. See the published version at https://doi.org/10.1038/s41467-023-38506-5.

Abstract

Sustainable production of acetic acid (AA) is a high priority due to its high global manufacturing capacity and numerous applications. Currently it is predominantly synthesized via carbonylation of methanol, in which both the reactants are fossil-derived. CO_2 transformation into AA is highly desirable to achieve net zero carbon emissions, but significant challenges remain to achieve this efficiently. Herein, we report a heterogeneous catalyst, thermally transformed MIL-88B with Fe^0 and Fe_3O_4 dual active sites, for highly selective AA formation via methanol hydrocarboxylation. This efficient catalyst showed high AA yield (590.1 mmol/g_{cat}.L) with 81.7% selectivity at 150°C in aqueous phase using LiI as a co-catalyst. The reaction is believed to proceed via formic acid intermediate. No significant difference in AA yield and selectivity was noticed during catalyst recycling study up to five cycles. This work scalable and industrially relevant for CO_2 utilisation to reduce carbon emissions, especially if green methanol and green hydrogen are used.

1. Introduction

Fixation of overabundant atmospheric carbon dioxide is an urgent and essential research area, which may lead towards climate mitigation. Several routes for carbon dioxide conversion have been investigated, but thermocatalytic CO_2 hydrogenation pathway is one of the major focus due to its fast kinetics, high productivity, scalability and selectivity [1]. Synthesis of chemicals such as methane[2, 3], methanol[4], formaldehyde[5, 6], dimethyl ether[7], gasoline-range hydrocarbons[8], oxymethylene dimethyl ethers[9, 10], methyl formate[11], formic acid[12], and acetic acid[13, 14] have been investigated in recent years. A CO_2 based chemicals industry has the potential to lower the CO_2 concentration in atmosphere, while simultaneously provide revenue for offsetting the capture costs. The production of acetic acid (AA) via CO_2 hydrogenation is one such route which is receiving attention of the researchers recently.

Acetic acid is extensively used in several industrial applications, including food, chemicals, pharmaceuticals, textile, cosmetics and polymers [15]. It is a well-known food preservative and traditionally named as vinegar in food industry. Commercially, two major production processes are used for the synthesis of acetic acid – chemical and fermentative [15, 16]. Among various chemical routes, the most common industrial processes are carbonylation of methanol (MeOH) developed by BASF, Cativa and Monsanto, in the presence of homogeneous Cobalt, Iridium and Rhodium catalysts, respectively. In Monsanto process, AA is produced from CH_3OH and fossil fuel derived CO in the presence of CH_3I and homogeneous rhodium-based catalyst[13, 15]. The main reaction of acetic acid production from methanol and CO is summarized in Eq. 1.

$$CH_3OH + CO \leftrightarrows CH_3COOH$$

1

Qian et al. recently reported AA production via hydrocarboxylation of MeOH with carbon dioxide and hydrogen in 1,3-dimethyl-2-imidazolidinone (DMI) solvent over homogeneous Rh and Ru based homogeneous co-catalysts with a combination of LiI promoter and imidazole ligand. While the authors report that imidazole played critical role in inhibiting the reverse water gas shift reaction, but the exact role of imidazole in the reaction mechanism was not clear[13]. The same group also showed AA synthesis via the above described reaction system in the presence of $Rh_2(CO)_4Cl_2$ homogeneous catalyst, LiCl as a co-catalyst, 4-methyl imidazole ligand and LiI as a promoter [17]. This reaction system is highly complex due to the presence of multiple catalysts, stabilizing ligands and organic solvents. In many cases, the authors report a black precipitate, which is not explained but is likely to be the Ru or Rh catalyst, which demonstrates that the system is not stable. Hasan et al. reported low yield of acetic acid (1.58 mmol/L) over NiO-C/Al_2O_3, heterogeneous catalyst at 130°C and 35 bar total pressure of CO_2 and H_2 in 1,4 dioxane solvent after 6h of reaction. Instead a higher amount of formic acid (FA, 4.08 mmol/L) was generated [18]. Therefore, there is an urgent need to develop a stable and active heterogeneous catalyst based on low cost metals for AA synthesis which can efficient for industrialisation and scaleup.

He et. al. report FA and AA production via hydrothermal CO_2 reduction with Fe nanoparticles as stoichiometric reagent in which they are converted into ferrous carbonate[19]. To the best of our knowledge, Fe-based heterogeneous catalysts have not been reported CO_2 conversion in aqueous phase. Heterogeneous catalysts have advantages in scale-up, and compares favourably against homogeneous catalysts which require large downstream separation processes.

Here we present a Fe-based thermally transformed metal organic framework catalyst (MIL-88B) for hydrocarboxylation of MeOH to produced AA. Recently, Metal Organic Framework (MOFs) derived carbonaceous materials have been reported for their remarkable catalytic properties[20, 21, 22]. Thermal transformation of MOFs results in a carbonaceous material with embedded metal or metal-oxide nanoparticles[22]. As these particles are embedded in the matrix of decomposed organic linkers, they show greater resistance to sintering at higher temperatures. Depending on the thermal treatment, the thermally transformed MOFs have features such as high surface area, porosity, and fine dispersion of metal nanoparticles that are desired in an ideal heterogeneous catalyst. Moreover, the porous carbon framework provides better mass transfer to enhance the reaction rate. In this work, thermally transformed MIL-88B, called T-MIL-88B, consisted of dual active sites – Fe^0 and Fe_3O_4, accelerating the conversion of CO_2 into AA, compared with other Fe-based catalysts tested which contained only Fe_3O_4 or Fe^0 and Fe_2O_3. In this process, AA is produced in a series of reactions (eq. 2-4) –

$$CO_{2(aq)} + H_{2(aq)} \underset{\longleftrightarrow}{\text{Fe}} HCOOH$$

2

$$CH_3OH_{(l)} + LiI \leftrightarrow CH_3I + LiOH$$

3

$$CH_3I + HCOOH + LiOH \leftrightarrow CH_3COOH + LiI + H_2O$$

4

Overall Reaction

$$CO_{2(aq)} + H_{2(aq)} + CH_3OH_{(l)} \xleftrightarrow{\text{Fe, LiI, } 150^\circ\text{C}} H_3CCOOH + H_2O$$

5

2. Methods

2.1. Materials

Iodomethane (CH_3I, 99.5%), formic acid (HCOOH, ≥ 95%), lithium Iodide (LiI, 99.9%), terephthalic acid (H_2BDC, 98%), chromium chloride hexahydrate ($CrCl_3.6H_2O$, 98%), and iron nitrate nonahydrate ($Fe(NO_3)_3.9H_2O$, 98%) were purchased from the Sigma Aldrich. Commercial zeolite-beta (CBEA, SiO_2/Al_2O_3= 38) was received from Zeolyst International. Methanol (HPLC grade) was obtained from the Scharlau Chemicals. Milli-Q water was used for catalysts synthesis (MIL-101 and Fe/CBEA) and acetic acid production experiments.

2.2. Catalysts synthesis

2.2.1. Fe/CBEA

Wet impregnation process was used for Fe/CBEA synthesis as described in our previous publication[9]. The loading of Fe was fixed as 10 wt% in this catalyst. Typically, $Fe(NO_3)_3.9H_2O$ (7.2 g) was dissolved in Milli-Q water (30 mL) by using 100 mL Schott bottle and stirred for 15 min at 65°C to prepare a homogeneous mixture of Fe solution. Thereafter, 9.0 g of CBEA support was immersed in this solution under stirring and maintained it for 6 h at the same temperature to achieve an even dispersion of Fe particles on CBEA support. The mixture was dried in oven at 100°C followed by calcination at 550°C with 5°C/min for 5 h in muffle furnace. The synthesised catalyst was reduced in the environment of H_2/Ar (1:1 v/v) gas mixture at 400°C for 5 h with heating rate of 5°C/min prior to carbon dioxide conversion experiment.

2.2.2. Thermally transformed Fe/MIL-101

10 mmol of H_2BDC and 10 mmol $CrCl_3.6H_2O$ were poured into a Teflon-lined autoclave. Subsequently, Milli-Q water (72 ml) was added to it. The reaction mixture was sonicated for 30 minutes followed by stirring for another 30 minutes at 500 rpm. Thereafter, the autoclave was kept in the oven at 205°C for 24 h and allowed to cool to room temperature. The resulting solid suspension was transferred into a centrifuge tube. Initially the centrifugation was performed at 1000 rpm for 3-4 min to remove the

unreacted H_2BDC present in the reaction mixture. Thereafter, the centrifugation was carried out at 5000 rpm for 10 minutes. The solid sample was then washed with dimethylformamide (DMF) three times and then dried in an oven at 70°C for 12 h. The synthesised material was named as MIL-101.

For Fe/MIL-101 synthesis, 2.7 g of MIL-101 was suspended in 70 ml ethanol in a Schott bottle and sonicated for 30 minutes. Separately, 2.17 g $Fe(NO_3)_3.9H_2O$ was dissolved in 20 ml ethanol in a different Schott bottle and stirred for 15 minutes. The latter solution was poured into the former suspension of MIL-101 in ethanol. Then the Schott bottle which contained $Fe(NO_3)_3$ solution was washed with 10 ml ethanol three times and poured into MIL-101 suspension to ensure complete transfer of the Fe precursor. The resultant mixture was sonicated for 30 min followed by stirring at 50°C at 500 rpm for 5-6 h. Finally, the resulting reaction mixture was dried in an oven at 80°C for 2-3 days. The synthesized catalyst was named as Fe/MIL-101. The Fe loading was fixed as 10 wt% in the synthesized catalyst. Prior to catalytic activity test, this catalyst was thermally transformed under 100 ml/min H_2/Ar (1:1) gas mixture at 500°C for 5 h with a heating rate of 5°C/min and allowed to cool in 50 ml/min Ar atmosphere and denoted as T-Fe/MIL-101.

2.2.3. Thermally transformed MIL-88B

A modified hydrothermal method as described in the literature[23] was adopted for synthesis of MIL-88B. In a typical procedure, 12.12 g of Fe salt ($Fe(NO_3)_3.9H_2O$) was dissolved in 75 ml DMF under stirring (500 RPM) in a Schott bottle. Separately, H_2BDC (4.98 g) and DMF (75 ml) were added in a 250 ml Teflon-liner under stirring (500 RPM). Both Fe and H_2BDC solutions were stirred further for 15 min at room temperature. The Fe solution was then poured into H_2BDC precursor solution. 12 ml NaOH solution (4.0 M) was slowly transferred into Fe and H_2BDC solution mixture and stirred again for 30 min at room temperature. Thereafter, the Teflon-liner was sealed in an autoclave and heated to 100°C for 24 h. After cooling to room temperature, MIL-88B particles were collected from this mixture via centrifugation at 7000 RPM for 10 min and washed three times with DMF and methanol, respectively. Finally, the as synthesized MIL-88B was dried overnight in the oven at 80°C and denoted as MIL-88B. Thermal transformation of MIL-88B (2 g) was conducted at 500°C for 5 h with a ramp of 5°C/min under 100 ml/min H_2/Ar (1:1 v/v) environment followed by cooling to room temperature under Ar at 50 ml/min atmosphere and denoted as T-MIL-88B.

2.3. Catalyst characterisation

The crystal structure of the materials was investigated with Powder X-ray diffraction (PXRD) by using a Rigaku MiniFlex device. The powder catalysts were loaded in a zero-background sample holder and scanned between 2–80° 2θ with 4°/min scan speed at 15 mA and 40 kV. Nitrogen physisorption analysis was conducted with Micromeritics 3Flex 3500 machine to find the type of adsorption isotherm, Brunauer-Emmett-Teller (BET) surface area and Barrett-Joyner-Halenda (BJH) pore distribution. Tecani T20 was used to capture the transmission electron microscopy (TEM) images of the catalysts. All the samples were dispersed in ethanol and immobilised onto the surface of a holy carbon grid followed by drying in

air prior to analysis. ThermoScientific K-Alpha machine was utilized for X-ray photoelectron spectroscopy (XPS) at 1486.6 eV Ephoton and coupled with monochromatic Al Kα radiations. The binding energy (B.E.) baseline correction was conducted by adjusting the C 1 s peaks at 284.8 eV. Thermally transformed samples were prepared *ex situ* prior to the XPS characterization. Shimadzu DTG-60H thermogravimetric analyser was used to check the thermal stability of Fe/MIL-101 and MIL-88B. Both samples were analysed in the temperature range of 100-800°C with a ramp of 5°C/min under Ar atmosphere.

2.4. Aqueous phase CO_2 conversion

All the aqueous phase CO_2 conversion experiments were performed in a 100 mL Teflon-lined autoclave batch reactor (Amar Equipment, M4). Typically, 0.4 g of thermally transformed catalyst (T-MIL-88B) and 40 mL water was added to the reactor and CH_3I (10 mmol) was carefully poured into it and sealed. It was purged with hydrogen three times to eliminate air from the headspace. The reactor was then pressurised with CO_2 up to 35 bar, followed by H_2 up to a total pressure of 70 bar at room temperature to achieve CO_2:H_2 ratio of 1:1. The reactor was heated to 150°C under continuous stirring at 200 RPM for 21 h. After 21 h of reaction, the reactor was allowed to cool to room temperature and the remaining gases were carefully vented from it before dissembling it. The catalyst was recovered from the liquid product mixture by centrifugation at 8500 RPM for 1 h. The same procedure was repeated for different total pressures at equimolar CO_2:H_2 ratio and different catalysts (T-Fe/MIL-101 and Fe/CBEA). The liquid sample was analysed at intervals for the best catalyst to check the extent of reaction against time at 150°C, equimolar CO_2:H_2 at 70 bar with 200 RPM stirring speed. The liquid samples were analysed using an HPLC (Agilent 1220 Infinity) equipped with a C18 column and a refractive index detector (RID), using 0.5 mM H_2SO_4 aqueous solution as the mobile phase. The product yields (mmol/g_{cat}.L) and selectivity (%) were calculated using equations 6 and7, respectively.

$$\mathrm{Product_i Yield} = \frac{\mathrm{n_i}}{\mathrm{m_{cat}}.\,\mathrm{V_{H_2O}}}$$

6

$$\mathrm{Productselectivity} = \frac{n_i}{\sum_i n_i} \times 100$$

7

Where n_i = moles of product, i = HCOOH or CH_3COOH, $\mathrm{m_{cat}}$ = mass of catalyst (g) and $\mathrm{V_{H_2O}}$ = volume of water (L)

The best catalyst was also evaluated for aqueous phase conversion using CO_2, H_2 and methanol (10 mmol) as reactants and lithium iodide (10 mmol) as the promoter. All other reaction conditions were identical to the above described procedure.

2.5. Catalyst recycling study

The catalyst recyclability was investigated using CO_2, H_2 and CH_3OH (10 mmol) as reactants and lithium iodide (10 mmol) as the promoter at 150°C, equimolar H_2/CO_2 with 70 bar pressure at room temperature and 200 RPM stirring speed. After each cycle, the catalyst was recovered from the product mixture via centrifugation at 8500 RPM for 1 h and without any intermediate treatment, resuspended into a fresh reaction mixture at the same initial conditions. After five cycles, the centrifuged catalyst was dried overnight in oven at 70°C and stored in air tight glass vial for its characterisation.

2.6. Reaction mechanism investigation

Reaction mechanism was explored by designing two different experiments – (1) using FA and CH_3I as reactants and experiment was conducted in water by using T-MIL-88B catalyst at 150°C under 35 bar hydrogen and 200 RPM stirring speed. Typically, 40 mL H_2O, 0.4 g of T-MIL-88B, 5 mmol (312.5 mmol/g_{cat}.L) of HCOOH and 10 mmol (625 mmol/g_{cat}.L) of CH_3I were added in Teflon-liner and reactor was sealed. After achieving the above described conditions, 2 mL liquid sample was withdrawn from the reactor after regular intervals (1, 2, 4, 8, 12 and 24 h) for HPLC analysis. In the 2nd reaction system, aqueous phase CO_2 hydrogenation with CH_3OH (10 mmol) and LiI (10 mmol) was performed over MIL-88B (0.4 g) for 48 h at 150 ˚C, 40 mL H_2O, equimolar H_2/CO_2 under 70 bar at room temperature and 200 RPM stirring speed. After 48 h, the reactor was cooled to room temperature. Both liquid and gas samples were collected for product analysis, where, gas sample was analysed through Shimadzu 2014 GC coupled with TCD and FID detectors, respectively.

3. Results And Discussion

3.1. Characterisation

Figure 1.a-c illustrates the PXRD diffractograms of the catalysts, before and after catalytic tests. Calcined Fe/CBEA catalyst showed characteristic peaks of α-Fe_2O_3, most of which were not observed in the reduced catalyst. Instead, the reduced catalyst showed Fe^0 peaks at 2θ = 44.7° and 65° and residual α-Fe_2O_3 peaks at 35.98° and 62.83°. However, there were no Fe^0 or α-Fe_2O_3 peaks detected in the used catalyst which indicated leaching of Fe from the catalyst support. The residual reaction solution slowly turned to red colour over a period of few days, indicating presence of iron oxides in the solution. Therefore, Fe/CBEA catalyst was not considered further.

Both the fresh and the used T-Fe/MIL-101 catalyst showed peaks corresponding to Fe_3O_4, suggesting that the catalyst was stable after the reaction. However, the α-Fe_2O_3 peaks observed in Fe/MIL-101 (Figure S1, ESI) which did not reduce to Fe^0 in T-Fe/MIL-101.

T-MIL-88B catalyst showed peaks corresponding to both Fe_3O_4 and Fe^0, which remained steady after a single run of 48 h reaction time and 5 cycles of 21 h each. Only Fe_3O_4 peaks have been reported after the thermal treatment of MIL-88B at 500°C under nitrogen atmosphere[23]. However, due to the reducing

atmosphere used in this study, some of iron oxide nanoparticles reduced to Fe^0. No evidence of iron carbide was found in the PXRD results.

During the thermal transformation of MOFs, first, the linkers break from the metal oxide clusters. After that, the metal oxide clusters agglomerate and reduce depending upon the chemical environment. MIL-88B consists Fe_3O clusters coordinated by six carboxylate ligands and three adsorbed water molecules, depending on the synthesis method (Figure 2a). Based on our earlier computational study of thermal transformations in Zr-based MOFs[24], we expect the following physiochemical transformations in MIL-88B upon thermal treatment. First, the adsorbed water molecules desorb, and at c.a. 100°C the MOF is expected to change the morphology[25]. Near the decomposition temperature, some of the linkers start detaching from the cluster. Unlike Fe oxide nanoparticles encapsulated in MIL-101(Cr), where the movement of nanoparticles is less hindered and can easily agglomerate, in MIL-88B, the Fe_3O metal clusters are part of the framework and hence remain less mobile. After detachment of the organic linkers, the linkers go through thermolysis, resulting in formation of small gaseous molecules such as CO and CO_2. At high temperature, hydrogen is expected to dissociate on iron and likely to catalyse the decarboxylation of linkers, reducing the Fe-O coordination. Without the oxygen from carboxylate groups, formation of single Fe_3O_4 phase is stoichiometrically not possible in Fe_3O. Hence, promoted decarboxylation in H_2 environment is likely to increase the abundance of a mixed Fe/Fe_3O_4 metal nanoparticles. Figure 2 shows the proposed mechanism of thermal evolution of MIL-88B(Fe).

Figure 3.a-f shows the TEM images of MIL-101, Fe/MIL-101, T-Fe/MIL-101, MIL-88B, T-MIL-88B, and used T-MIL-88B, respectively. MIL-101 shows the characteristic octahedral shape of ca. 200-300 nm size (Figure 3a and Figure S2a of ESI)[26]. After impregnation of Fe over MIL-101, agglomerates of Fe nanoparticles were observed on MIL-101 (Fe/MIL-101) with approximately 50-100 nm in size (Figure 3b), whereas after thermal transformation, T-Fe/MIL-101 exhibited approximately 5-30 nm particles (Figure 3c). The emergence of these smaller nanoparticles is likely due to the thermal transformation of Fe/MIL-101 in reductive atmosphere, where the deconstruction of linkers leads to breakage of the Fe agglomerates. Figure 3d and Figure S2b (ESI) show the characteristic fusiform rod shaped morphology of MIL-88B with ~360 nm length and 90 nm width[23]. After thermal transformation, T-MIL-88B shows a narrow range of Fe^0/Fe_3O_4 nanoparticle which are well-dispersed over the carbonaceous support (Figure 2e). The amount of Fe on T-MIL-88B is 49.3%, with 13.7% C and negligible amount of H, N and S (Table S1, ESI), which indicates that original MOF structure is completely transformed into porous carbon. Figure 3f shows that the T-MIL-88B catalyst retains its structure after 48h of reaction. Figure 3.g-h illustrates the particle size distribution (PSD) for T-MIL-88B and used T-MIL-88B, respectively. 525 and 476 particles were measured from multiple images which showed most of the particles in 4-16 nm for both fresh and used T-MIL-88B, respectively. The peaks were observed at 8 nm with average particle sizes of 9.7 and 9.1 nm for fresh and used T-MIL-88B, respectively which suggested that the studied catalyst is stable and potentially reusable for this reaction.

The surface oxidation state of Fe in the different catalysts was evaluated by X-Ray photoelectron spectroscopy (XPS) study, as shown in Figure 4. For T-MIL-88B (Figure 4.a), Fe $2p_{3/2}$ XPS spectrum exhibited three peaks, including a peak at 706.9 eV corresponding to metallic iron [27]. Moreover, the other two peaks at 710.1 and 712.3 eV which are correlated to Fe^{+2} and Fe^{+3} oxidation state of iron and the satellite peaks for these aforementioned oxidation state appeared at 716.6 and 719.8 eV [28]. In the Fe 2p region of T-MIL-88B, $Fe2p_{1/2}$ and $Fe2p_{3/2}$ peaks are situated 710.1 and 723.8 eV, where, the spin orbital splitting is 13.7 eV that indicated the presence of Fe_3O_4 in T-MIL-88B [29]. Fe_3O_4 may exist as mixed FeO and Fe_2O_3 states, which appears from Fe^{+2} and Fe^{+3} oxidation states [30]. The present XPS study shows that Fe_3O_4 is the dominant species on the surface, where the amount of Fe^{+2} was 60.4% and Fe^{+3} was 21.0%, whereas Fe^0 was 18.6%. Therefore, the ratio of Fe^0 to Fe_3O_4 was accounted as 1/4.38 in T-MIL-88B.

The XPS spectra of Fe $2p_{3/2}$ in T-Fe/MIL-101 exhibited two peaks at 711.7 and 712.4 eV which is related to Fe^{+2} and Fe^{+3} along with two satellite peaks at 718.1 and 722.4 eV. Furthermore, $Fe2p_{1/2}$ and $Fe2p_{3/2}$ of Fe^{+2} appeared at 711.7 and 725.4 eV and the spin orbital splitting is 13.7 eV which interpreted the existence of Fe_3O_4 in T-Fe/MIL-101. Metallic Fe peak is absent in this catalyst which is in good agreement with PXRD results. For Fe/MIL-101 catalyst, Fe $2p_{3/2}$ XPS spectra also contained both Fe^{+2} and Fe^{+3} at 711.7 and 713.4 eV, respectively. However, the spin orbit splitting for $Fe2p_{1/2}$ and $Fe2p_{3/2}$ is 14.1 eV (711.7 and 725.8 eV) which suggested the absence of Fe_3O_4 phase.

Figure 4b represented the Cr XPS spectra of MIL-101, Fe/MIL-101 and T-Fe/MIL-101 catalysts. In MIL-101, Cr 2p XPS spectra contained only one peak at 577.6 eV which is corresponds to Cr^{+3} oxidation state[31]. For Fe/MIL-101, Cr XPS spectra attributed to two peaks at 577.2 and 578.8 eV which are mainly resembles with Cr^{+3} and CrO_3 [32]. The negative binding energy shift (0.4 eV) of Cr^{+3} as compared to Cr^{+3} present in MIL-101 is most likely due to the interfacial electronic interaction (charge transfer) between Cr and Fe after the inclusion of Fe in MIL-101[28]. The Cr spectra for T-Fe/MIL-101, Cr XPS spectra mainly consisted with Cr^{+3} peak at 577.1 eV and the amount of CrO_3 is very less as compared to Fe/MIL-101 which may be due to the thermal transformation of Fe/MIL-101 under hydrogen atmosphere that reduces the oxidised Cr species on catalyst surface.

The C 1s XPS spectra for Fe/MIL-101 (Figure 3c) shows three different types of C peak at 285, 286.4 and 288.5 which belongs to C-C, C-O-C and O-C=O[33]. The C 1s XPS spectra of both T-Fe/MIL-101 and T-MIL-88B contains only two peaks corresponding to C-C and C-O-C, whereas, the O-C=O peak is absent, which may be due to the thermal transformation of both Fe/MIL-101 and MIL-88B under hydrogen atmosphere reducing the oxygen content in the catalyst.

A thermogravimetric analysis of Fe/MIL-101 and MIL-88B has been represented in Figure 5. For Fe/MIL-101, the weight loss in the range of 50-250°C is because of the evaporation of water and removal of free terephthalates inside the pore of MOF[34]. Thereafter, the main weight loss in the temperature range of 270

to 670°C is due to the degradation of organic ligand in the framework of MOF which is attributed to the collapse of the framework[34]. The weight loss of MIL-88B before 250°C corresponds to the removal of water and excess DMF from the framework[35]. For MIL-88B, the weight loss occurs in the temperature ranges of 300 to 500°C due to the degradation of H_2BDC and the breakdown of the framework. The step in the TGA profile of between 550-650°C is most likely due to the carbonization of the framework and the formation of Fe_3O_4–carbon composites[35].

3.2. Catalyst Activities

3.2.1. Role of Fe based zeolite and MOF catalysts

Figure 6.a-c illustrates the yield and selectivity of AA via aqueous phase CO_2 reduction with iodomethane at various pressures. All the catalysts showed some activity for AA production; however, T-MIL-88B was clearly the most active and selective catalyst with best yield of 504 mmol/g_{cat}.L and AA selectivity of 92.4%. Based on stoichiometric calculation, it is equivalent to 80.6% conversion of CH_3I into AA. Both Fe/CBEA and T-Fe/MIL-101 provide lower activity for CO_2 hydrogenation and >90% selectivity for FA production. With increasing pressure, the yield increased initially but the AA selectivity peaked at 60 bar for both Fe/CBEA and T-Fe/MIL-101. However, the AA yield and selectivity increases with increasing pressure for T-MIL-88B. Since Fe was present in the structural framework of T-MIL-88B, the thermally transformed catalyst consists of - embedded active metal sites dispersed evenly in a carbon matrix[23]. The high AA activity and the selectivity over T-MIL-88B catalyst is most likely due to the presence of both Fe^0 and Fe_3O_4 which assist the hydrogenation and C-C coupling reactions, respectively[36, 37].

3.2.2. Extent of reaction with time

Figure 7.a illustrates the extent of reaction over T-MIL-88B to produce AA and FA via CO_2 hydrogenation with CH_3I as the starting material in the aqueous media. The reaction proceeds via formation of FA as the initial product, whereas AA was not detected until after 8h of reaction. The AA yield and selectively sharply increased between 12 to 24 h, thereafter gradually increasing to 657.6mmol/g_{cat}.L and 98.8%, respectively, at 48h as the reaction approached equilibrium conversion. Based on the initial CH_3I concentration (10 mmol), 100% conversion at 100% selectivity for AA was achieved, within the range of measurement errors. However, as discussed later, CO_2 first converts into FA and after reaching the maximum yield (377.4 mmol/g_{cat}.L) at 8h, the FA yield decreases sharply until the end of reaction at 48 h when the FA yield was measured at 8.1 mmol/g_{cat}.L. However, since CH_3I is consumed by this time, the residual FA cannot convert into AA. Therefore, for the CO_2 hydrogenated into carboxylic acids, the selectivity of AA is 98.8%.

When CH_3OH (10 mmol) was used as a reactant with LiI as a co-catalyst (Figure 7b), in otherwise identical reaction conditions, the reaction generates *in situ* CH3I and hence the peak of FA is broader than Figure 7a. The AA yield and selectivity increased more gradually and achieved a similar yield of 590.1

mmol/g_{cat}.L at 81.7% selectivity after 48 h, which is equivalent to 94% conversion of CH3OH into AA. The *in-situ* production of CH_3I slowed down the conversion of FA into AA, which may be due to mass transfer limitation.

3.2.3. Catalyst reusability

Figure 8 shows that the catalytic activity dropped initially but after three cycles, there was no significant decline in AA yield and selectivity. The PXRD of the used catalyst after five cycles (Figure 1.c), and the TEM image (Figure 3.f) and PSD (Figure 3.h) of used catalyst after 48 h confirmed that the structure is stable and there was no sintering or agglomeration of Fe and Fe_3O_4 nanoparticles in T-MIL-88B. The initial loss in activity is likely due to the loss of small particles of the catalyst which could not be recollected in centrifuge.

3.2.4. Proposed Reaction Pathway

Reaction mechanism of hydrocarboxylation of methanol in an organic solvent proceeds via reaction of CH_3OH with LiI to produce CH_3I and LiOH which is similar to the carbonylation of methanol (Monsanto processes) followed by formation of CH_3Rh^*I due to the insertion of CH_3I into a Rh* complexing catalyst [13]. Further, CO_2 is inserted into CH_3-Rh bond to produce CH_3COORh^*I. Finally, CH_3COOH is formed via reduction of CH_3COORh^*I with H_2 molecule in the presence of Ru* to produce HI as an intermediate. Whereas, LiI is regenerated in situ via HI formation which reacts with LiOH to produce H_2O and LiI. However, here we show aqueous phase methanol hydrocarboxylation in which the reaction pathway deviates from the published works and FA is formed as an intermediate.

First, we show that FA can react with CH_3I in water over T-MIL-88B in H_2 atmosphere (Figure 9). The conversion of FA closely follows AA yield and after 24 h of the reaction FA conversion of 91.5% is achieved with 100% AA selectivity.

Next, we show aqueous phase hydrocarboxylation of CH_3OH using T-MIL-88B as catalyst and LiI as co-catalyst. Here both liquid and gas samples were collected after 48 of reaction. The liquid sample showed only the presence of HCOOH and CH_3COOH with 81.7% acetic acid selectivity (Figure 7.b). Whereas gas analysis did not detect any carbonaceous molecules apart from CO_2 (ESI, Figure S4), which eliminates the methanol carbonylation route for AA production.

Figure 10 shows the proposed reaction pathway for acetic acid production via hydrocarboxylation of CH_3OH over T-MIL-88B. CO_2 and H_2 adsorbed over the catalyst and converted into FA, which may desorb. Subsequently, the adsorbed formate species reacts with iodomethane (CH_3I) to allow C-C coupling reaction to take place which generates an acetate species and HI as the by-product. Finally, acetate species is converted into acetic acid, whilst LiI might be regenerated from LiOH and HI (step 8).

4. Conclusions

We show that thermally transformed Fe-based metal organic framework-based catalyst (T-MIL-88B) exhibited high catalytic activity and stability for aqueous phase CO_2 transformation into acetic acid. Here, the catalytic activity and the structural property of T-MIL-88B was compared with Fe/CBEA and thermally transformed Fe deposited on MIL-101 (T-Fe/MIL-101). The T-MIL-88B consisted both Fe^0 and Fe_3O_4 phases, which catalyse hydrogenation and C-C coupling reactions, respectively, making this catalyst superior to the others tested here. Using CH_3OH, CO_2 and H_2 as reactants in aqueous phase, and LiI the promoter, a maximum acetic acid yield of 590.1 mmol/g_{cat}.L, with 81.7% selectivity was achieved after 48 h at 150 ˚C. We propose that the hydrocarboxylation of methanol to make acetic acid is mediated by formate route, which is evidenced by formic acid as an intermediate. The T-MIL-88B catalyst was active for at least five cycles for acetic acid production without showing any signs of deactivation via sintering, oxidation or phase change.

Declarations

Acknowledgement

Authors would like to thank the Faculty of Engineering, Monash University for financial support under the Researcher Accelerator Grant 2019. Authors would also acknowledge Monash Centre for Electron Microscopy (MCEM) for providing the microscopic analysis facilities. AT and AS received financial support from the Institute for Catalysis, Hokkaido University as part of their Strategic Research Fellowship grant scheme. This study was supported by the Cooperative Research Program of Institute for Catalysis, Hokkaido University (Proposal no. 19A1005).

References

1. Li W, *et al.* A short review of recent advances in CO 2 hydrogenation to hydrocarbons over heterogeneous catalysts. *RSC advances* **8**, 7651–7669 (2018).
2. Ahmad W, Younis MN, Shawabkeh R, Ahmed S. Synthesis of lanthanide series (La, Ce, Pr, Eu & Gd) promoted Ni/γ-Al2O3 catalysts for methanation of CO2 at low temperature under atmospheric pressure. *Catalysis Communications* **100**, 121–126 (2017).
3. Ahmad W, Al-Matar A, Shawabkeh R, Rana A. An experimental and thermodynamic study for conversion of CO2 to CO and methane over Cu-K/Al2O3. *Journal of environmental chemical engineering* **4**, 2725–2735 (2016).
4. Rui N, Wang Z, Sun K, Ye J, Ge Q, Liu C-j. CO2 hydrogenation to methanol over Pd/In2O3: effects of Pd and oxygen vacancy. *Applied Catalysis B: Environmental* **218**, 488–497 (2017).
5. Lee DK, Kim DS, Kim SW. Selective formation of formaldehyde from carbon dioxide and hydrogen over PtCu/SiO2. *Applied organometallic chemistry* **15**, 148–150 (2001).
6. Chan FL, Altinkaya G, Fung N, Tanksale A. Low temperature hydrogenation of carbon dioxide into formaldehyde in liquid media. *Catalysis Today* **309**, 242–247 (2018).

7. Frusteri F, Cordaro M, Cannilla C, Bonura G. Multifunctionality of Cu–ZnO–ZrO2/H-ZSM5 catalysts for the one-step CO2-to-DME hydrogenation reaction. *Applied Catalysis B: Environmental* **162**, 57–65 (2015).
8. Gao P, *et al.* Direct conversion of CO 2 into liquid fuels with high selectivity over a bifunctional catalyst. *Nature Chemistry* **9**, 1019–1024 (2017).
9. Ahmad W, Chan FL, Hoadley A, Wang H, Tanksale A. Synthesis of oxymethylene dimethyl ethers (OMEn) via methanol mediated COx hydrogenation over Ru/BEA catalysts. *Applied Catalysis B: Environmental* **269**, 118765 (2020).
10. Siebert M, Krennrich G, Seibicke M, Siegle AF, Trapp O. Identifying high-performance catalytic conditions for carbon dioxide reduction to dimethoxymethane by multivariate modelling. *Chemical science* **10**, 10466–10474 (2019).
11. Corral-Pérez JJ, *et al.* Decisive Role of Perimeter Sites in Silica-Supported Ag Nanoparticles in Selective Hydrogenation of CO2 to Methyl Formate in the Presence of Methanol. *Journal of the American Chemical Society* **140**, 13884–13891 (2018).
12. Preti D, Resta C, Squarcialupi S, Fachinetti G. Carbon dioxide hydrogenation to formic acid by using a heterogeneous gold catalyst. *Angewandte Chemie* **123**, 12759–12762 (2011).
13. Qian Q, Zhang J, Cui M, Han B. Synthesis of acetic acid via methanol hydrocarboxylation with CO 2 and H 2. *Nature communications* **7**, 1–7 (2016).
14. Hasan S, Ahmad K, Isahak W, Masdar M, Jahim J. Synthesis of low-cost catalyst NiO (111) for CO2 hydrogenation into short-chain carboxylic acids. *International Journal of Hydrogen Energy* **45**, 22281–22290 (2020).
15. Pal P, Nayak J. Acetic acid production and purification: critical review towards process intensification. *Separation & Purification Reviews* **46**, 44–61 (2017).
16. Ndoye B, Lebecque S, Destain J, Guiro AT, Thonart P. A new pilot plant scale acetifier designed for vinegar production in Sub-Saharan Africa. *Process Biochemistry* **42**, 1561–1565 (2007).
17. Cui M, Qian Q, Zhang J, Chen C, Han B. Efficient synthesis of acetic acid via Rh catalyzed methanol hydrocarboxylation with CO 2 and H 2 under milder conditions. *Green Chemistry* **19**, 3558–3565 (2017).
18. Hasan S, Ahmad K, Isahak W, Pudukudy M, Masdar M, Jahim J. Synthesis, Characterisation and Catalytic Activity of NiO supported Al2O3 for CO2 Hydrogenation to Carboxylic Acids: Influence of Catalyst Structure. In: *IOP Conference Series: Earth and Environmental* Science). IOP Publishing (2019).
19. He C, Tian G, Liu Z, Feng S. A mild hydrothermal route to fix carbon dioxide to simple carboxylic acids. *Organic letters* **12**, 649–651 (2010).
20. Lippi R, *et al.* Highly active catalyst for CO2 methanation derived from a metal organic framework template. *Journal of Materials Chemistry A* **5**, 12990–12997 (2017).
21. Lippi R, *et al.* Unveiling the structural transitions during activation of a CO2 methanation catalyst Ru0/ZrO2 synthesised from a MOF precursor. *Catalysis Today* **368**, 66–77 (2021).

22. Alqarni DS, *et al.* Ru-zirconia catalyst derived from MIL140C for carbon dioxide conversion to methane. *Catalysis Today* **371**, 120–133 (2021).
23. Liu J, *et al.* Fe-MOF-derived highly active catalysts for carbon dioxide hydrogenation to valuable hydrocarbons. *Journal of CO2 Utilization* **21**, 100–107 (2017).
24. Dwivedi S, *et al.* Atomistic Mechanisms of Thermal Transformation in a Zr-Metal Organic Framework, MIL-140C. *The Journal of Physical Chemistry Letters* **12**, 177–184 (2021).
25. Horcajada P, *et al.* How Linker's Modification Controls Swelling Properties of Highly Flexible Iron(III) Dicarboxylates MIL-88. *Journal of the American Chemical Society* **133**, 17839–17847 (2011).
26. Zhao M, *et al.* Metal–organic frameworks as selectivity regulators for hydrogenation reactions. *Nature* **539**, 76–80 (2016).
27. Ma Z, Song T, Yuan Y, Yang Y. Synergistic catalysis on Fe–Nx sites and Fe nanoparticles for efficient synthesis of quinolines and quinazolinones via oxidative coupling of amines and aldehydes. *Chemical science* **10**, 10283–10289 (2019).
28. Koley P, *et al.* Leveraging Cu/CuFe2O4-Catalyzed Biomass-Derived Furfural Hydrodeoxygenation: A Nanoscale Metal–Organic-Framework Template Is the Prime Key. *ACS applied materials & interfaces* **12**, 21682–21700 (2020).
29. Lee H, Lee W-J, Park Y-K, Ki SJ, Kim B-J, Jung S-C. Liquid phase plasma synthesis of iron oxide nanoparticles on nitrogen-doped activated carbon resulting in nanocomposite for supercapacitor applications. *Nanomaterials* **8**, 190 (2018).
30. Madhuvilakku R, Alagar S, Mariappan R, Piraman S. Green one-pot synthesis of flowers-like Fe3O4/rGO hybrid nanocomposites for effective electrochemical detection of riboflavin and low-cost supercapacitor applications. *Sensors and Actuators B: Chemical* **253**, 879–892 (2017).
31. Huo Q, *et al.* Preparation of a direct Z-scheme α-Fe2O3/MIL-101 (Cr) hybrid for degradation of carbamazepine under visible light irradiation. *Applied Catalysis B: Environmental* **255**, 117751 (2019).
32. Guo L, Qin S, Yang B, Liang D, Qiao L. Effect of hydrogen on semiconductive properties of passive film on ferrite and austenite phases in a duplex stainless steel. *Scientific reports* **7**, 1–6 (2017).
33. Fen-rong L, Wen L, Hui-qing G, Bao-qing L, Zong-qing B, Rui-sheng H. XPS study on the change of carbon-containing groups and sulfur transformation on coal surface. *Journal of Fuel Chemistry and Technology* **39**, 81–84 (2011).
34. Liu Z, He W, Zhang Q, Shapour H, Bakhtari MF. Preparation of a GO/MIL-101 (Fe) Composite for the Removal of Methyl Orange from Aqueous Solution. *ACS omega*, (2021).
35. Hou S, *et al.* Green synthesis and evaluation of an iron-based metal–organic framework MIL-88B for efficient decontamination of arsenate from water. *Dalton transactions* **47**, 2222–2231 (2018).
36. Zhang L, Chen X, Peng Z, Liang C. Chemoselective hydrogenation of cinnamaldehyde over MOFs-derived M2Si@ C (M= Fe, Co, Ni) silicides catalysts. *Molecular Catalysis* **449**, 14–24 (2018).

37. Zeng T, Chen W-W, Cirtiu CM, Moores A, Song G, Li C-J. Fe 3 O 4 nanoparticles: a robust and magnetically recoverable catalyst for three-component coupling of aldehyde, alkyne and amine. *Green Chemistry* **12**, 570–573 (2010).

Figures

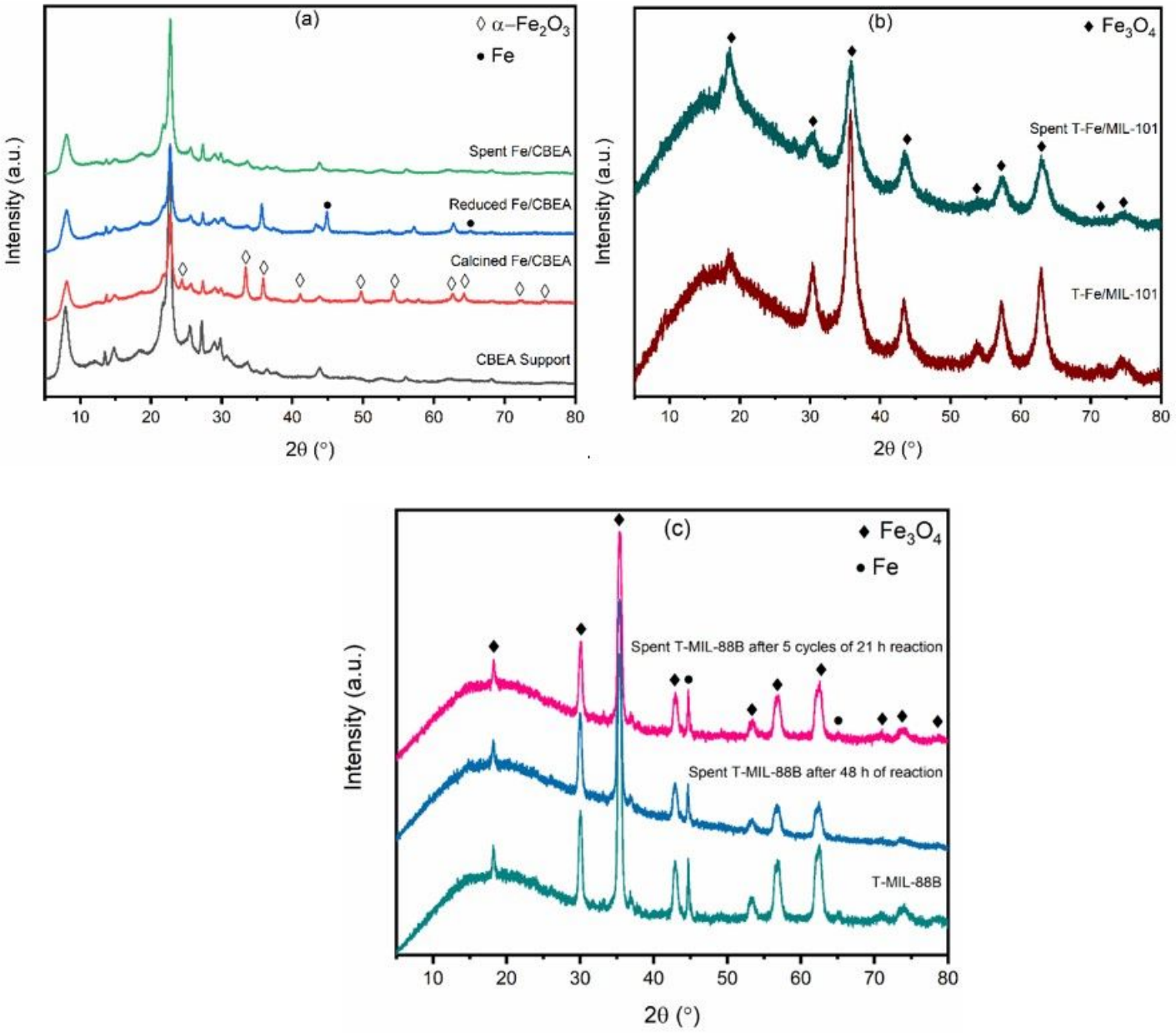

Figure 1

PXRD patterns of (a) as prepared, calcined, reduced and used Fe/CBEA, (b) as prepared and used T-Fe/MIL-101, and (c) as prepared and used T-MIL-88B catalysts after 48 h reaction in presence of CH3I and 5 cycles of 21 h each in presence of CH3OH and LiI.

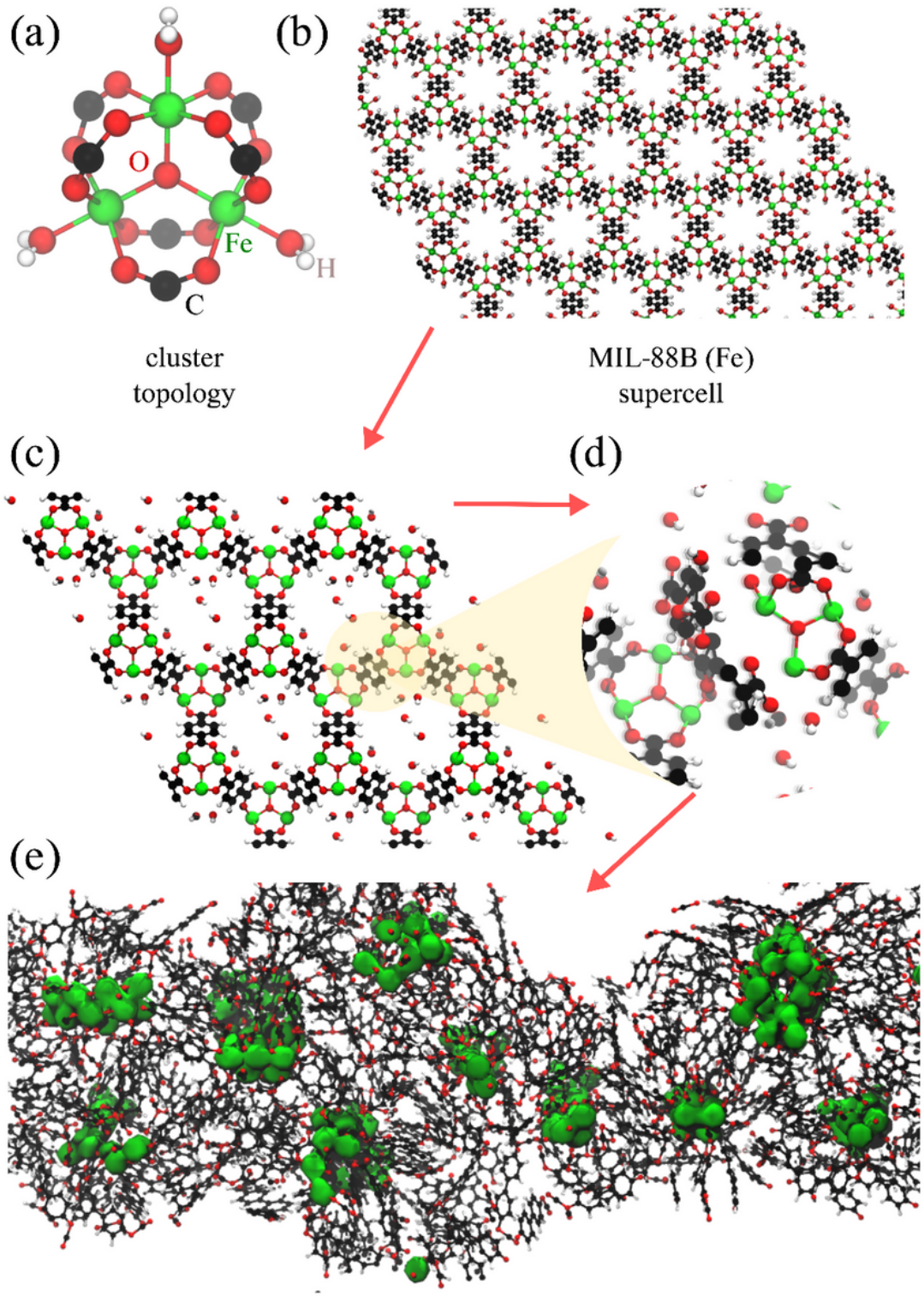

Figure 2

Proposed mechanism of thermal transformation of MIL-88B(Fe) structure. (a) Shows the metal cluster topology, (b) shows MOF supercell structure, (c) desorbed water molecules within the pores of MOF, (d) shows the detachment of organic linkers, and (e) is the thermally transformed MIL-88B(Fe).

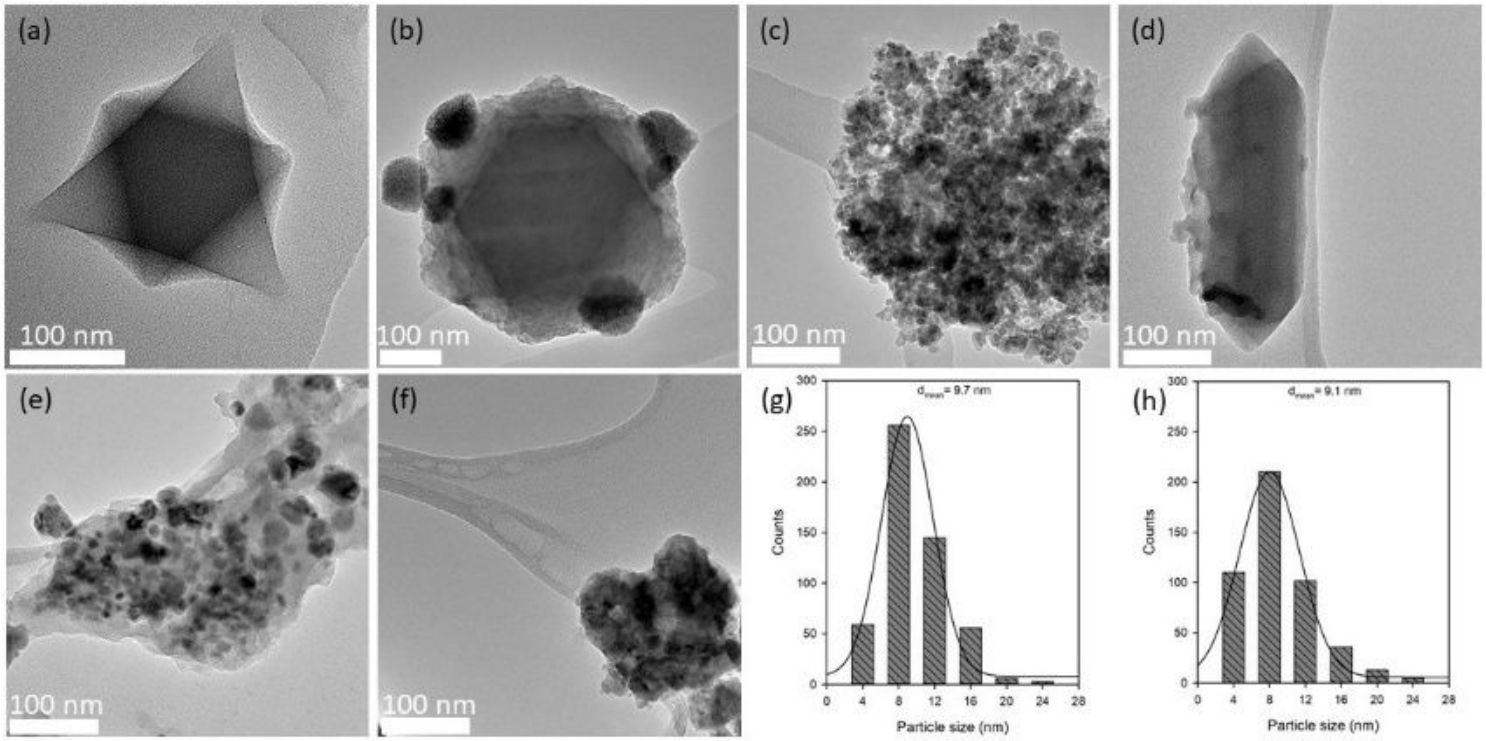

Figure 3

TEM micrographs of various studied catalysts, (a) MIL-101, (b) Fe/MIL-101, (c) T-Fe/MIL-101, (d) MIL-88B, (e) T-MIL-88B, and (f) used T-MIL-88B after 48 h of aqueous phase CO2 hydrogenation reaction in the vicinity of CH3OH and LiI additives; and particle size distribution of (g) T-MIL-88B, and (h) used T-MIL-88B.

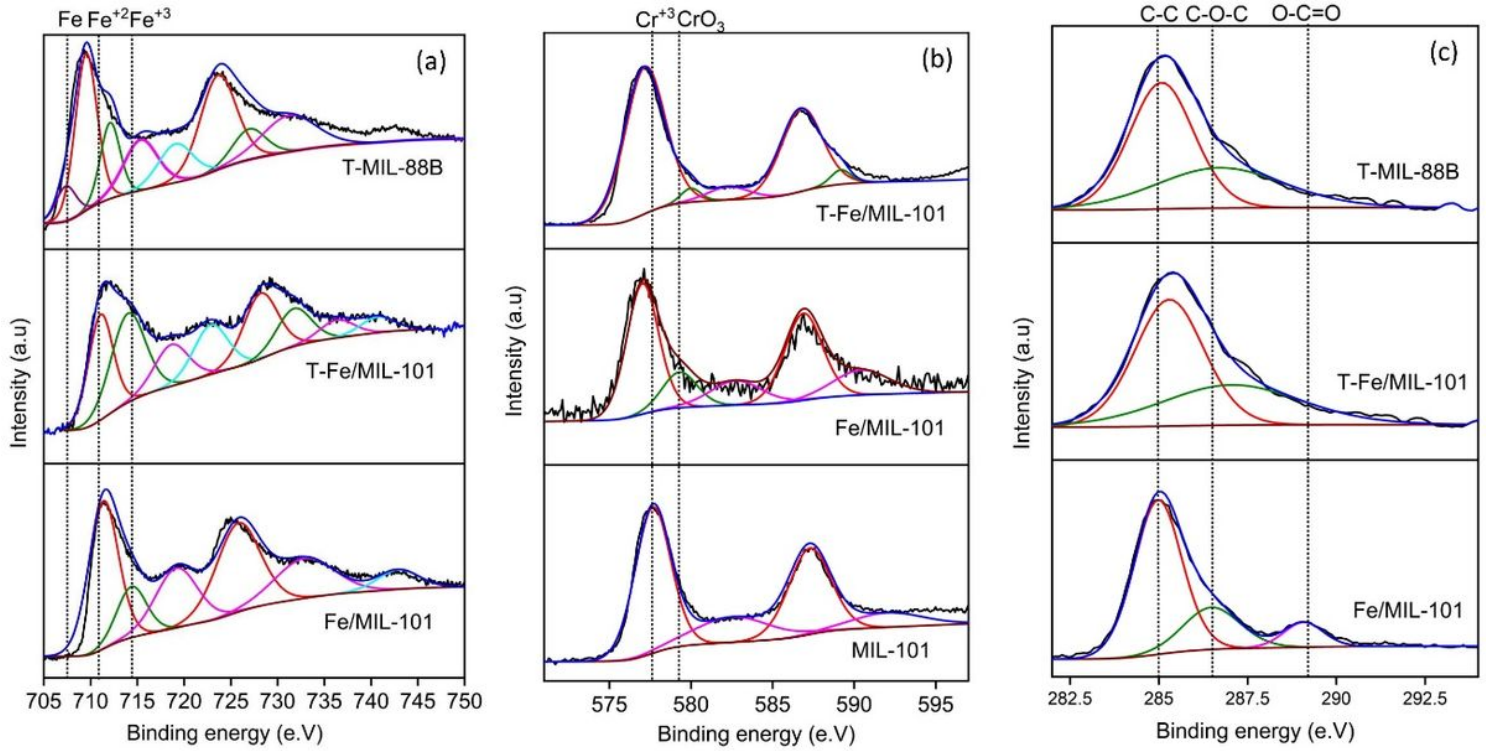

Figure 4

Narrow scan XPS spectra of (a) Iron 2p, (b) Chromium 2p, and (c) Carbon 1s for the studied catalysts.

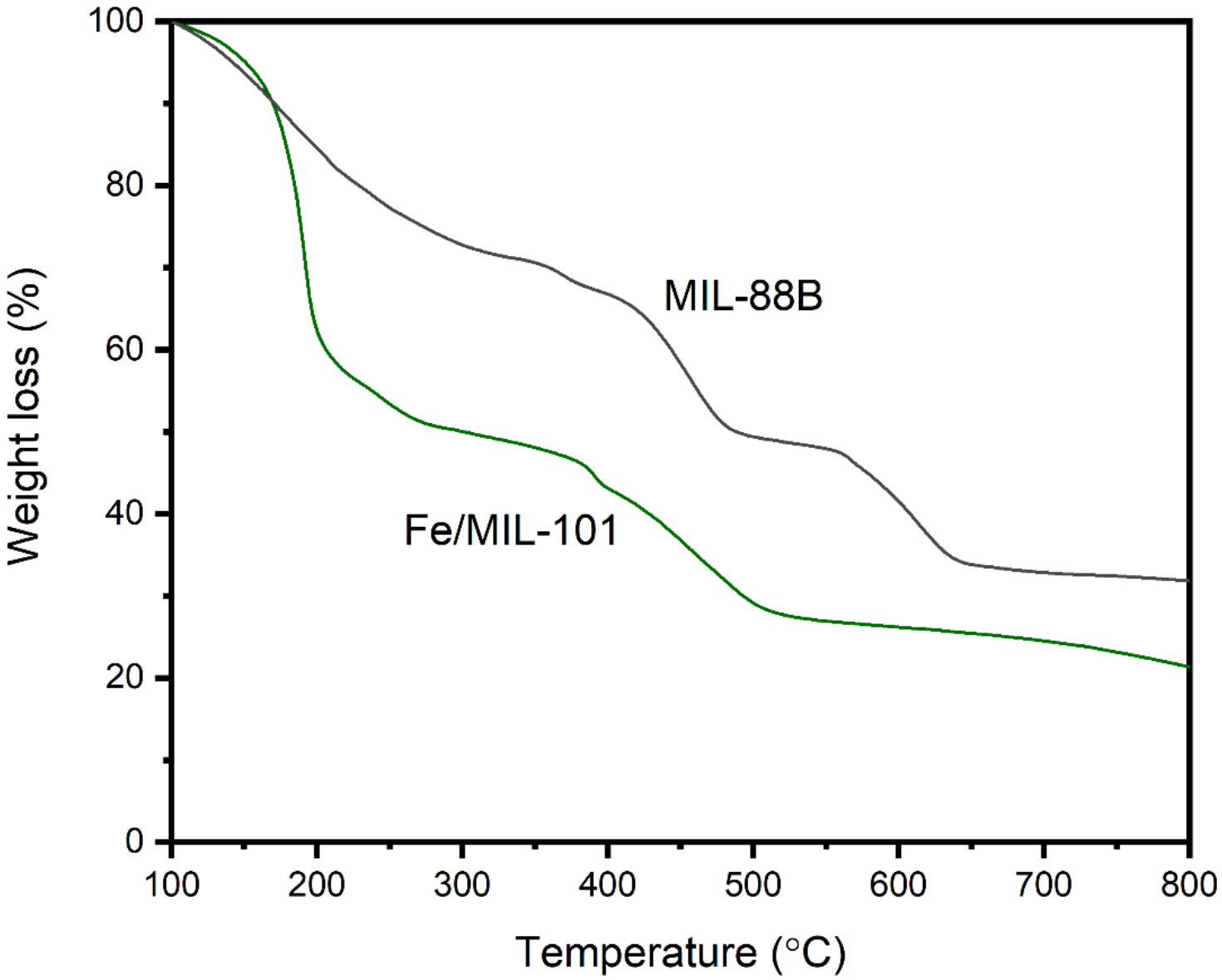

Figure 5

Thermogravimetric analysis (TGA) of Fe/MIL-101 and MIL-88B under Argon atmosphere.

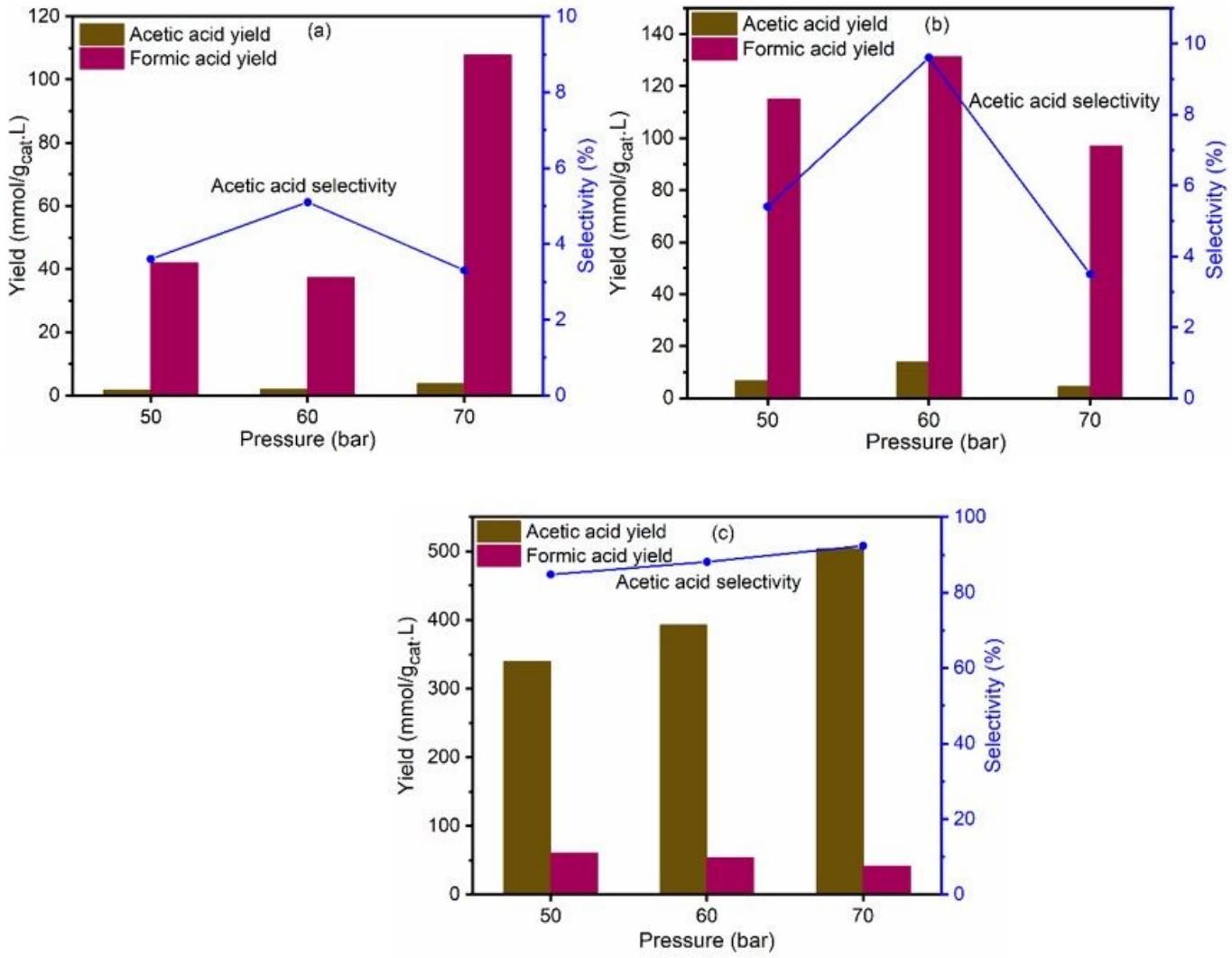

Figure 6

Activity of various Fe based catalysts during aqueous phase CO2 hydrogenation in the presence of CH3I additive at different pressure, (a) Fe/CBEA, (b) T-Fe/MIL-101, and (c) T-MIL-88B. Reaction conditions: T= 150 ˚C, H2/CO2= 1, tR= 21 h, H2O= 40 mL and stirring speed= 200 RPM.

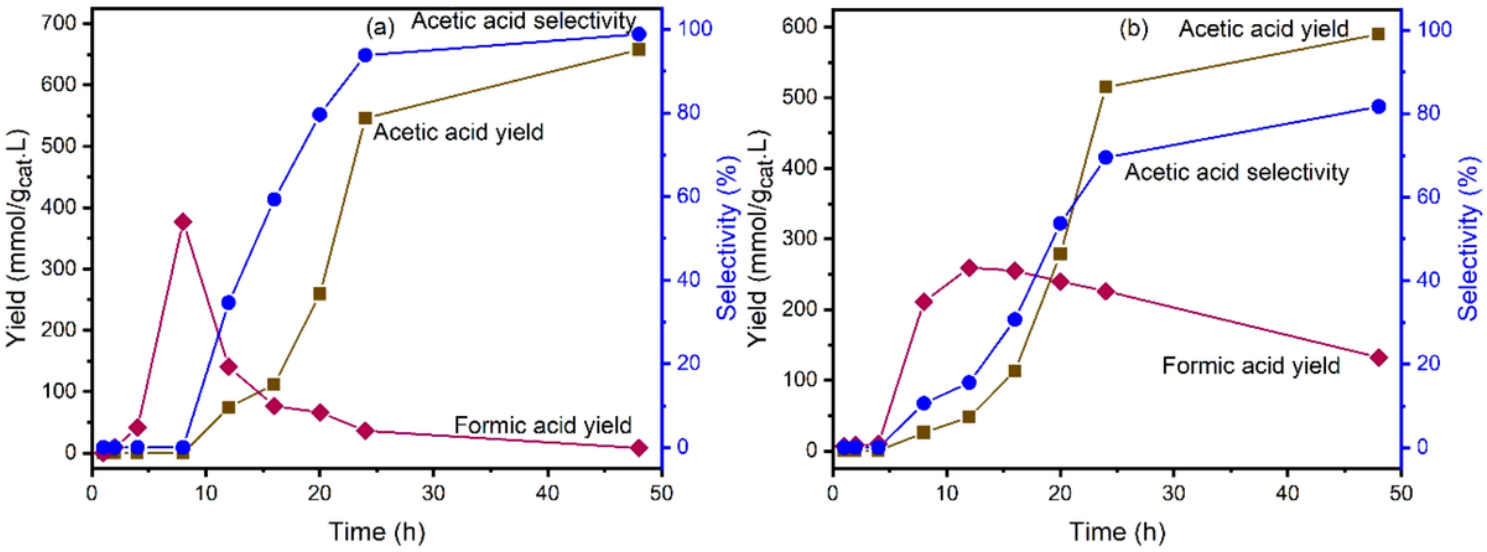

Figure 7

Effect of reaction time on carboxylic acids yield and selectivity via aqueous phase CO2 hydrogenation over T-MIL-88B in the presence of various additives, (a) CH3I, and (b) CH3OH and LiI. Reaction conditions: T= 150 ˚C, H2/CO2= 1, Ptotal= 70 bar at room temperature and stirring speed= 200 RPM.

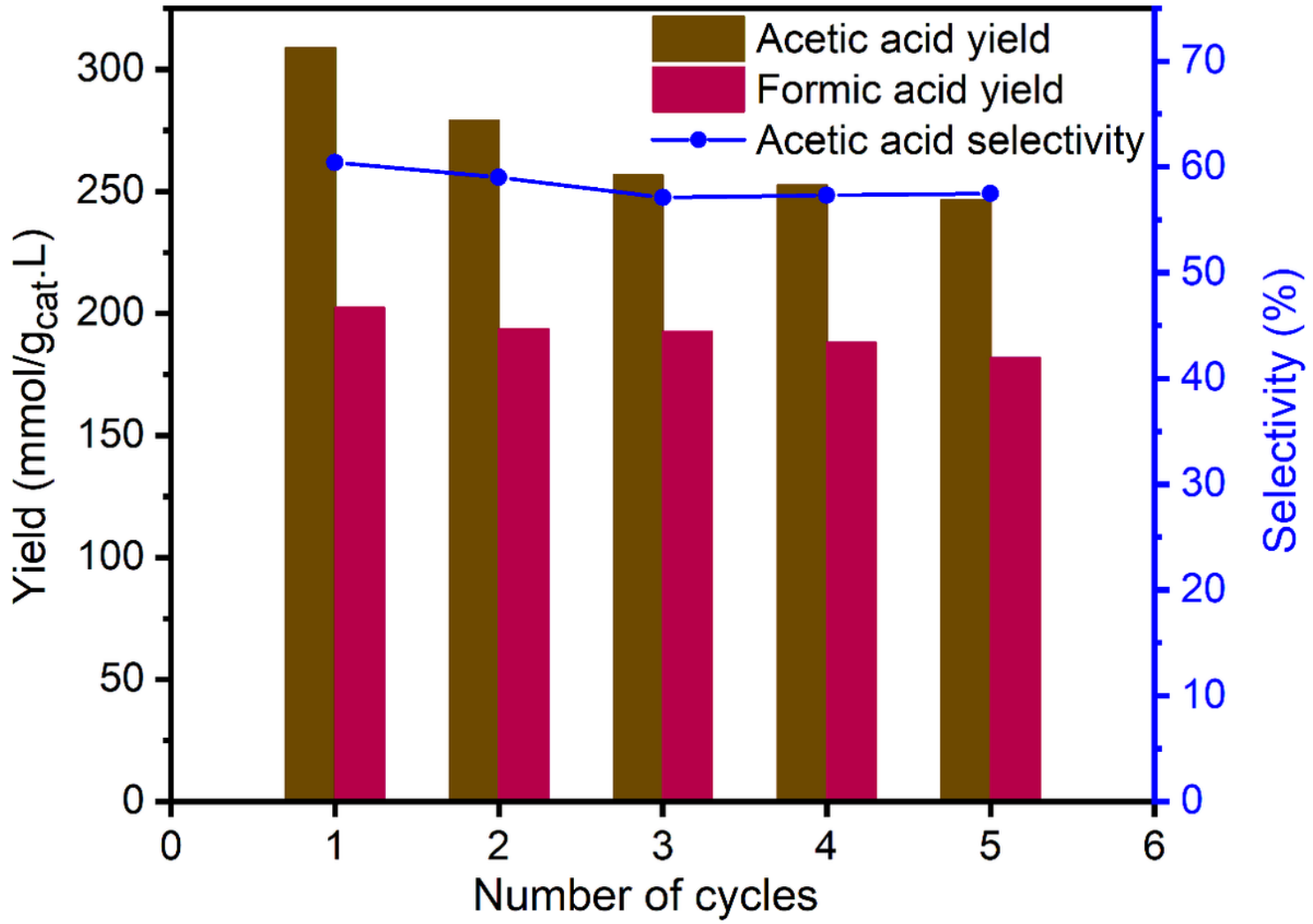

Figure 8

Recycling study of T-MIL-88B via aqueous phase CO2 hydrogenation in the presence of CH3OH and LiI additives. Reaction conditions: T= 150 ˚C, H2/CO2= 1, tR= 21 h, Ptotal= 70 bar at room temperature and stirring speed= 200 RPM.

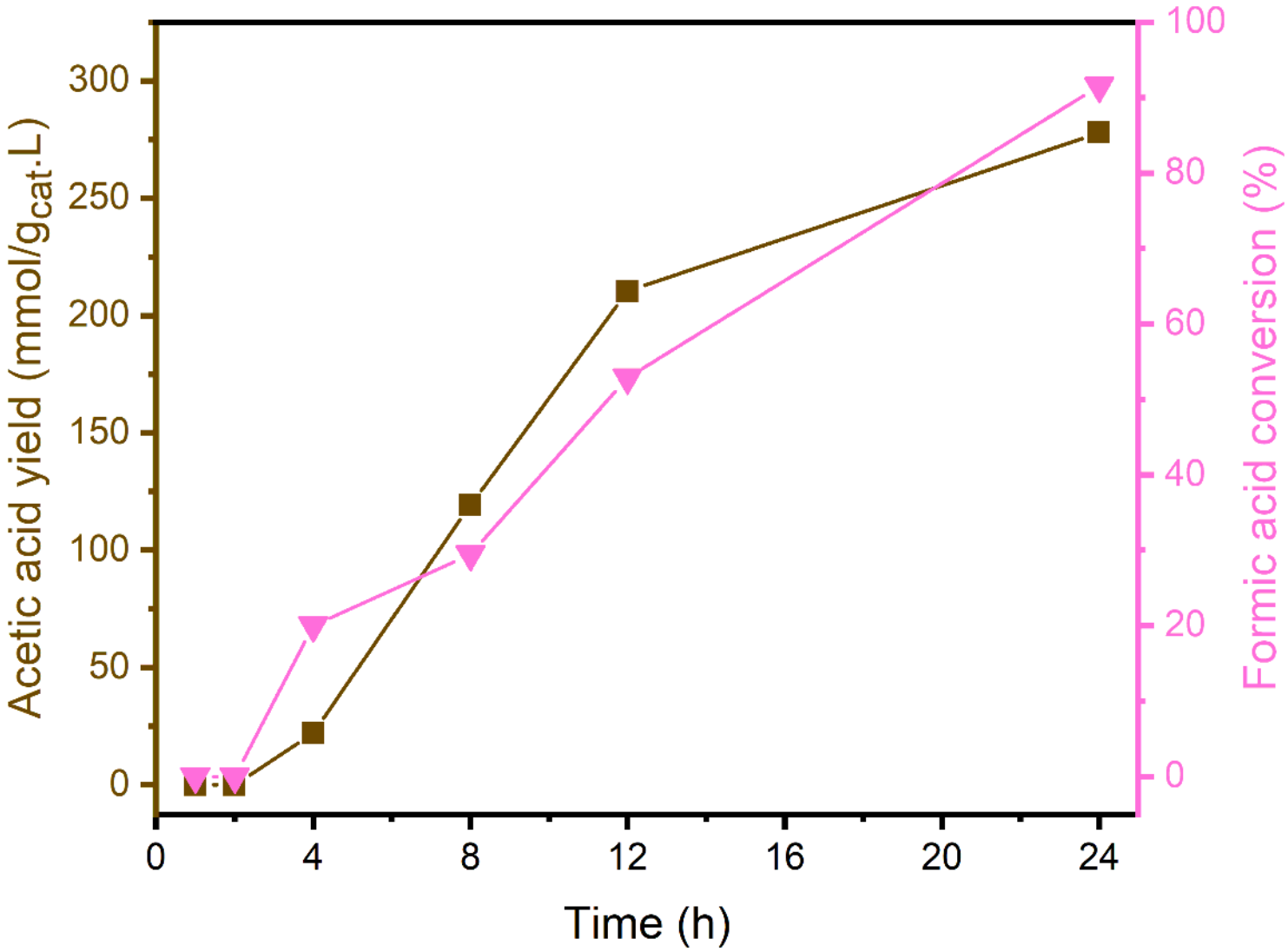

Figure 9

Acetic acid production through HCOOH and CH3I reaction in water over T-MIL-88B in the presence of hydrogenation. Reaction conditions: T= 150 ˚C, nHCOOH=5 mmol, nCH3I=10 mmol, VH2O=40 mL, PH2=35 bar at room temperature and stirring speed= 200 RPM.

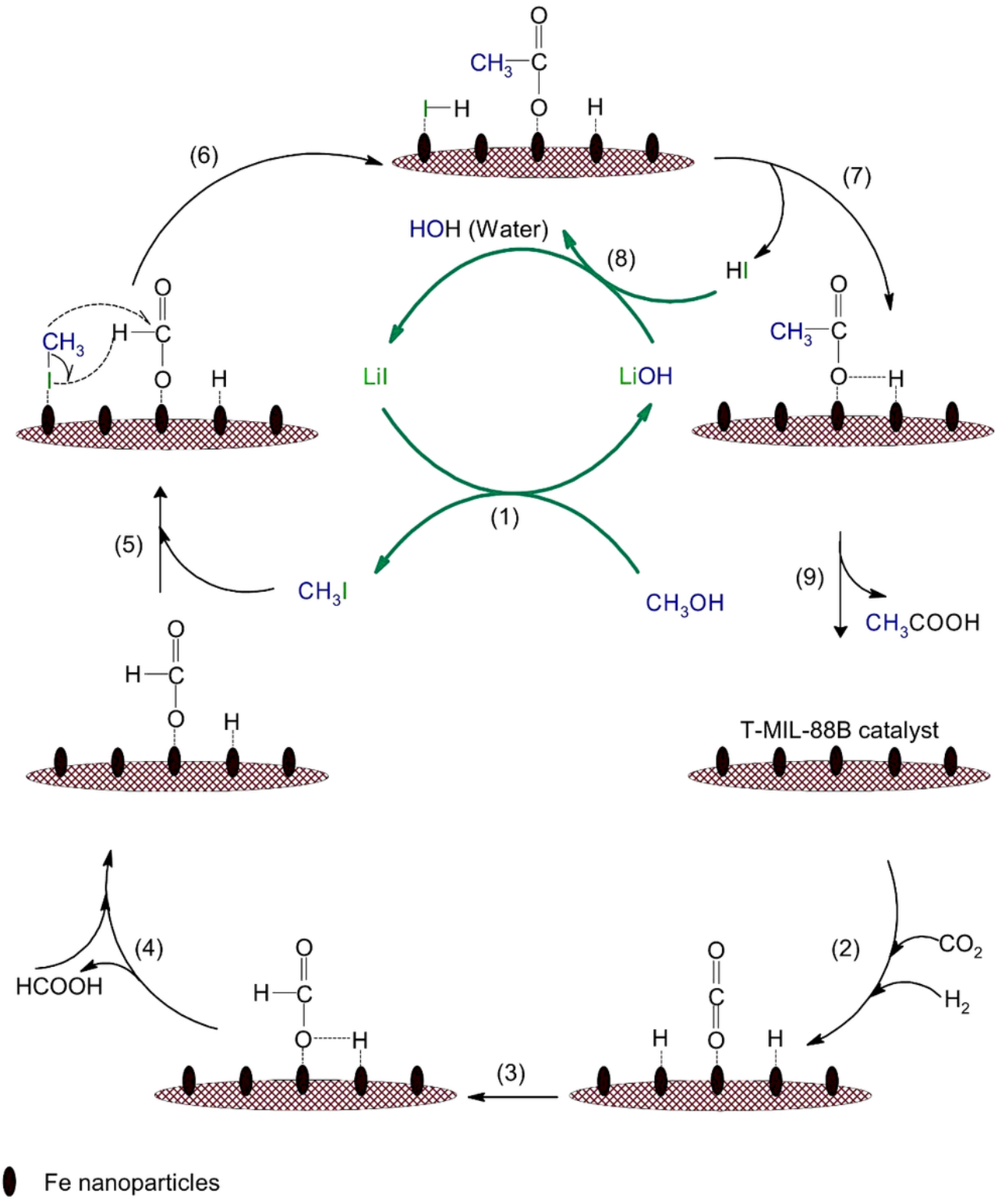

Figure 10

Possible reaction route for acetic acid production via aqueous phase CO2 hydrogenation in the vicinity of methanol and LiI additives over T-MIL-88B catalyst.

Supplementary Files

This is a list of supplementary files associated with this preprint. Click to download.

- 20211025AceticAcidManuscriptESI.docx